



# A seismic discontinuity in the upper mantle between the Eastern Alps and the Western Carpathians: Constraints from wide angle reflections and geological implications

T. Oeberseder<sup>a</sup>, M. Behm<sup>a,\*</sup>, I. Kovács<sup>b</sup>, G. Falus<sup>b</sup>

<sup>a</sup> Vienna University of Technology, Institute of Geodesy and Geophysics, Austria

<sup>b</sup> Eötvös Loránd Geophysical Institute of Hungary, Hungary

## ARTICLE INFO

### Article history:

Received 31 August 2010

Received in revised form 3 March 2011

Accepted 12 March 2011

Available online 21 March 2011

### Keywords:

Lithosphere

Upper mantle

Western Carpathians

Vienna Basin

Eastern Alps

Wide-angle reflection

## ABSTRACT

Seismic investigation of the lithosphere by means of active source experiments is mostly confined to the crust and the Moho. Structures in the upper mantle are more likely to be discovered by analyses of teleseismic data, although these methods are restricted in their resolution capabilities. The relatively rare evidence for upper mantle refractors or reflectors in active source data enables challenging and interesting studies of the lower and not so well known part of the lithosphere. We present such an example from the tectonically complex region between the Eastern Alps and the Western Carpathians. This area was covered by several extensive 3D wide-angle reflection/refraction experiments within the last decade, and their layout was designed to illuminate the crustal structure and in particular the Moho discontinuity. In some areas, reflections from below the Moho are also recorded. These reflections occur at recording offsets between 200 and 500 km, and they are particularly strong in cross line recordings. We derive a set of travel times from the data and perform a tomographic inversion for the depth and shape of the reflecting interface. The inversion makes use of an existing 3D crustal model which also includes the Moho topography. Since the upper mantle velocities are poorly constrained and the azimuthal distribution of the rays is biased, several tests are applied to investigate the reliability of possible solutions. The results from the tomographic inversion indicate an overall horizontal and radially dipping reflector. The average depth of the reflector is 55 km, which is about 25 km below the crust–mantle transition, and amplitude modelling suggests that the reflecting interface represents a velocity increase. The investigated area is further characterised by deep sedimentary basins, high heat flow, high velocities in the lower crust, diffuse Moho signature and a strong positive Bouguer anomaly. Nearby xenolith outcrops exhibit a pronounced change in anisotropy and indicate the presence of two distinct layers in the lithospheric mantle, whereas the deeper layer is thought to present more juvenile lithosphere derived from thermal relaxation in the post-extension phase. Most likely the upper mantle reflector also represents this change in anisotropy, though other scenarios are also possible. We conclude that the entire lithosphere is significantly shaped by extensional processes which affect the area since the late Oligocene/early Miocene.

© 2011 Elsevier B.V. All rights reserved.

## 1. Introduction

The existence of seismic discontinuities in the uppermost mantle is demonstrated in several datasets throughout the world. A shallow lithosphere–asthenosphere boundary (LAB) may cause significant reflectivity (Posgay et al., 1990, 1995). Balling (2000) gives a fine example of subducted oceanic crust which, after the transformation to eclogite, represents a steeply dipping high-velocity/density contrast. A similar mechanism is assumed for the well-known Flannan Reflector (Brewer et al., 1983; Price et al., 1996). North- and south-dipping mantle reflectors are imaged in the MONA LISA dataset from

the North Sea region (Mona Lisa Working Group, 1997). Abramovitz et al. (1998) interpreted these reflectors as a Caledonian subduction zone and a subsequently formed compressional shear zone. Carbonell (2004) found evidence for a reflective lithosphere and a less reflective asthenosphere from a high-density wide-angle shot gather in the Urals. Okure and McBride (2006) investigate a gently dipping mantle reflector below the Illinois Basin and provided two possible explanations. It either represents a deformation caused by a 1.6 Ga old subduction process or laminated lithosphere related to melting of proterozoic crust. Based on wide-angle data, Sfoda et al. (2006) image a steeply north-dipping reflector (in a depth range from 40 to 60 km) below the Carpathian foredeep and interpreted it as a shear zone resulting from the collision of the European Platform and the ALCAPA unit. As shown, possible causes for reflectivity in the uppermost mantle are widespread. Steer et al. (1998) offer four different

\* Corresponding author. Tel.: +43 58801 12822.

E-mail address: [mbehm@mail.tuwien.ac.at](mailto:mbehm@mail.tuwien.ac.at) (M. Behm).

explanations (remnant subduction zones, shear zones, fluids and seismic anisotropy) and discuss their significance for geodynamic interpretations.

The presented study aims at the interpretation of wide-angle reflections from within the uppermost mantle in the area between the Eastern Alps and the Western Carpathians.

## 2. Tectonic and geological setting

The investigated area (Fig. 1) is situated in between four different geological provinces: The Bohemian Massif in the North West, the Eastern Alps in the West, the Pannonian basin in the South East and the Western Carpathians in the North East. While the genesis of the Bohemian Massif dates back to the Paleozoic (e.g. [Matte et al., 1990](#)), the other provinces are related to alpine orogeny and subsequent processes (e.g. [Csontos and Vörös, 2004](#); [Horváth et al., 2006](#); [Schmid et al., 2004, 2008](#)). During the Eocene, about 50 Ma ago, a continent–continent-collision started between the European and Adriatic–Apulian plates, leading to the formation of the Alps. The Eastern Alps were subject to eastward directed lateral extrusion starting from the Late Oligocene (i.e., [Fodor and Csontos, 1999](#); [Horváth et al., 2006](#); [Ratschbacher et al., 1991](#)). The extrusion was facilitated by the eastward directed retreat of the Carpathian subduction which was active from the Early Miocene to Pliocene times. Since this subduction ceased, the actual stress regime in the region has changed from extensional to compressional due to the ongoing movement and

rotation of the Adriatic–Apulian plate ([Bada and Horváth, 2007](#)). The genesis of the Pannonian basin system is thought to be strongly related to the Carpathian subduction and its roll-back effect (i.e., [Horváth et al., 2006](#)). Cenozoic sedimentary fillings of this large basin system are up to 8 km thick. Its north-westernmost parts, the Vienna Basin, the Danube basin, and the Little Hungarian Plain represent the transition between the Eastern Alps and the Western Carpathians.

The inner Western Carpathians (i.e. south of the Penninic units) and the intervening portion of the Pannonian basin north of the Middle Hungarian zone (MHZ) are usually referred to as the ALCAPA block because of lithologic and stratigraphic similarities (e.g., [Csontos and Vörös, 2004](#); [Haas and Mioc, 2000](#); [Kovács and Szederkényi, 2000](#)). To its south, the ALCAPA block is separated from the Tisza–Dacia unit by the MHZ. While the ALCAPA block is derived from the Adriatic–Apulian Domain, the Tisza–Dacia unit is believed to have rifted off the European margin during the Late Jurassic.

[Kovács and Csontos \(2007\)](#) and [Kovács and Szabó \(2008\)](#) provide an overview of concurring ideas on the tectonic evolution of the area. Previous interpretations are in favour of a southward subduction of the European plate beneath the Western Carpathians. However, recent geophysical investigations ([Grad et al., 2006](#); [Szafian and Horváth, 2006](#)) could not show significant crustal thickening or southward dipping reflectors in the crust beneath the Western Carpathians. The volcanic rocks in the northern part of the Pannonian Basin (referred to as the “Western segment” in [Kovács and Szabó, 2008](#)) do not show a spatial and temporal pattern which would be

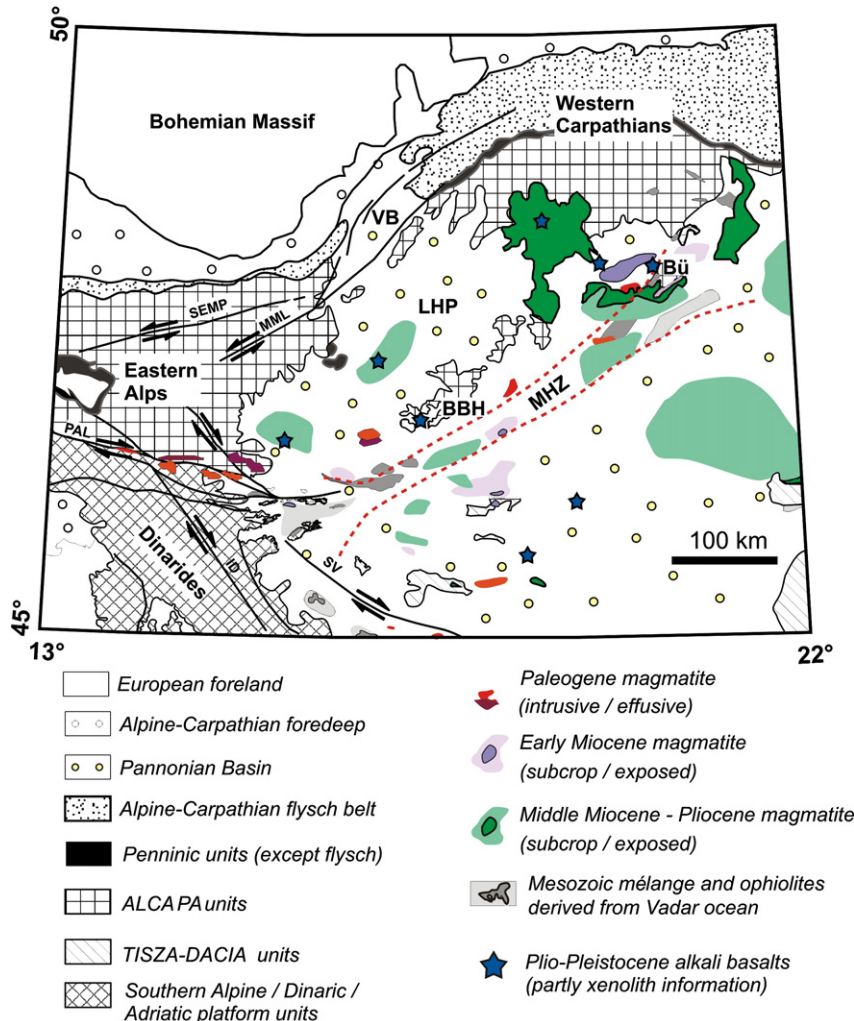


**Fig. 1.** Tectonic map of the investigated area. Solid lines: Major faults, active since early Miocene. SEMP: Salzachtal–Ennstal–Mariagezell–Puchberg – line. MML: Mur–Mürz – line. PAL: Periadriatic line. SV: Sava fault. ID: Idria fault. MHZ: Mid-Hungarian zone. VB: Vienna Basin. LHP: Little Hungarian Plain. Bü: Bükk Mountains. BBH: Bakony–Balaton Highlands.

expected if they were derived or generated by a subduction along the Western Carpathians. This is in contrast to the Eastern Carpathians where the European lithosphere is likely to have subducted below the Tisza–Dacia plate (i.e., [Seghedi and Downes, 2004](#)). Based on these litho-stratigraphic correlations and geochemical characteristics of igneous rocks, [Kovács and Szabó \(2008\)](#) postulate a geodynamic model for the Western Carpathians which focuses on strike-slip tectonics, rather than a convergence (i.e. subduction) dominated setting. In this model, the entire lithosphere of the ALCAPA block was brought to its present-day position via extrusions and rotations. The extension caused melting in the upper mantle and mafic underplating at the Moho, as evidenced by mafic cumulate xenoliths from the Bakony–Balaton Highland and Nógrád–Gömör area ([Embey-Isztin and Scharbert, 1990](#); [Kovács et al., 2004](#)). From a geophysical and tectonic perspective, [Brückl et al. \(2010\)](#) also emphasised strike-slip dominated tectonics on a lithospheric scale for the region between the Tauern Window in the Eastern Alps and the Vienna Basin. In their model, the ALCAPA and the Tisza units merged into the single lithospheric block “Pannonia” around the early Pliocene.

### 3. Data

The dataset used for analysis was compiled from the 3rd deployment of the CELEBRATION 2000 and the ALP 2002 experiments ([Brückl et al., 2003](#); [Guterch et al., 2003](#)). These wide-angle refraction/reflection experiments targeted the crustal structure and, in particular, the Moho topography. The average shot charge was 300 kg of explosives, and receiver spacing was 3 km on high density lines and 6 km on low density lines.

The investigated subset covers a 600×660 km wide area ([Fig. 2](#)) and comprises 78,894 traces, of which about 20% are in-line data. On some of the recording profiles (CEL01, CEL07, CEL09, CEL10, and CEL15) phases with strong amplitudes are clearly observable at offsets between 250 and 500 km ([Fig. 3](#)). These arrivals differ from the first arrival refractions from the upper mantle (Pn), which are observed at lower offsets (100–250 km) and arrive significantly earlier. Further-

more, the wavelets are more reverberant than the Pn phase. Similar events are found in wide-angle data throughout the world (e.g. [Hrubcová et al., 2005](#); [Majdański et al., 2006](#); [Nielsen and Thybo, 2009](#); and references in the previous section) and are commonly attributed to reflections from within the uppermost mantle.

The observed arrivals can be classified into two phases. The majority (denoted as “PIP”) clusters at offsets between 250 and 350 km. Only at a few record sections additional arrivals (“R2”) occur at much larger offsets (350 km to 450 km). Mostly, the R2 arrivals are separated by gaps in distance and time (0.5–1.0 s later in the LMO reduced sections) from the PIP arrivals. Thus they may result from a second, deeper reflecting horizon. In the following, we concentrate on the PIP arrivals. Their signal-noise ratio is generally high, which indicates a pronounced contrast in seismic impedance. Further on, the limited offset range (approx. 250 to 350 km) could be explained by an increased reflectivity coefficient at the critical offset, which in turn requires a velocity increase below the reflecting interface. This is further elaborated in [Section 6](#). Hypothetically, variations in the reflectivity coefficient due to its offset-dependency could also explain the offset gap between the PIP and R2 phases, if both are associated with the same reflecting horizon. But to further account for the time gap and the rare occurrence of R2 phases, a deeper reflector provides a simpler explanation.

We calculated the amplitude spectra of different phases for a single shot ([Fig. 4](#)). The Fourier transformation was applied to the individual traces after defining 2–3 s long time gates which include the entire wavelet, and the obtained spectra of the traces were stacked for each phase. The used shot was located in the Pannonian basin, and the Pg phases were recorded at relatively short offsets and thus also in low-velocity sediments. The other phases were recorded at larger offsets, mostly outside the basin. This explains the fact that the Pg phase has a relatively low frequency. The comparison of the reflected waves indicates a shift towards lower frequencies corresponding to the depth of the reflector (PmP, PIP, R2). The observed peaks at 9 Hz (PIP) and 6 Hz (R2) agree well with the results obtained by [Posgay et al. \(1990\)](#) who postulate that reflections from within the deep

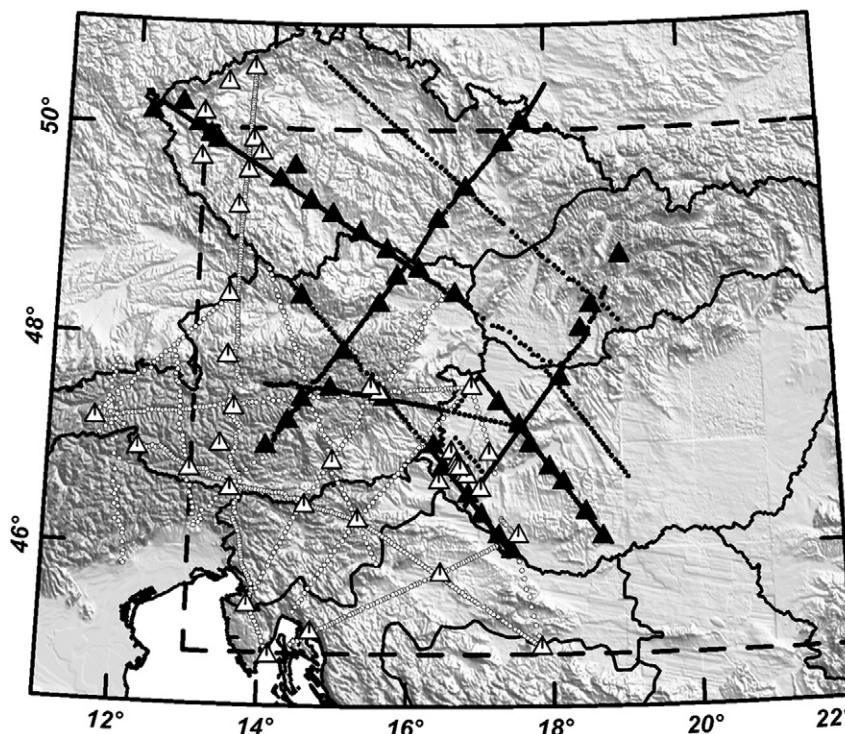


**Fig. 2.** Layout of the seismic experiments in the investigated area. Triangles: Shots; Dots: Receivers. White: ALP 2002 experiment. Black: CELEBRATION 2000 experiment. Inserted rectangle: Area of the geological map ([Fig. 1](#)).

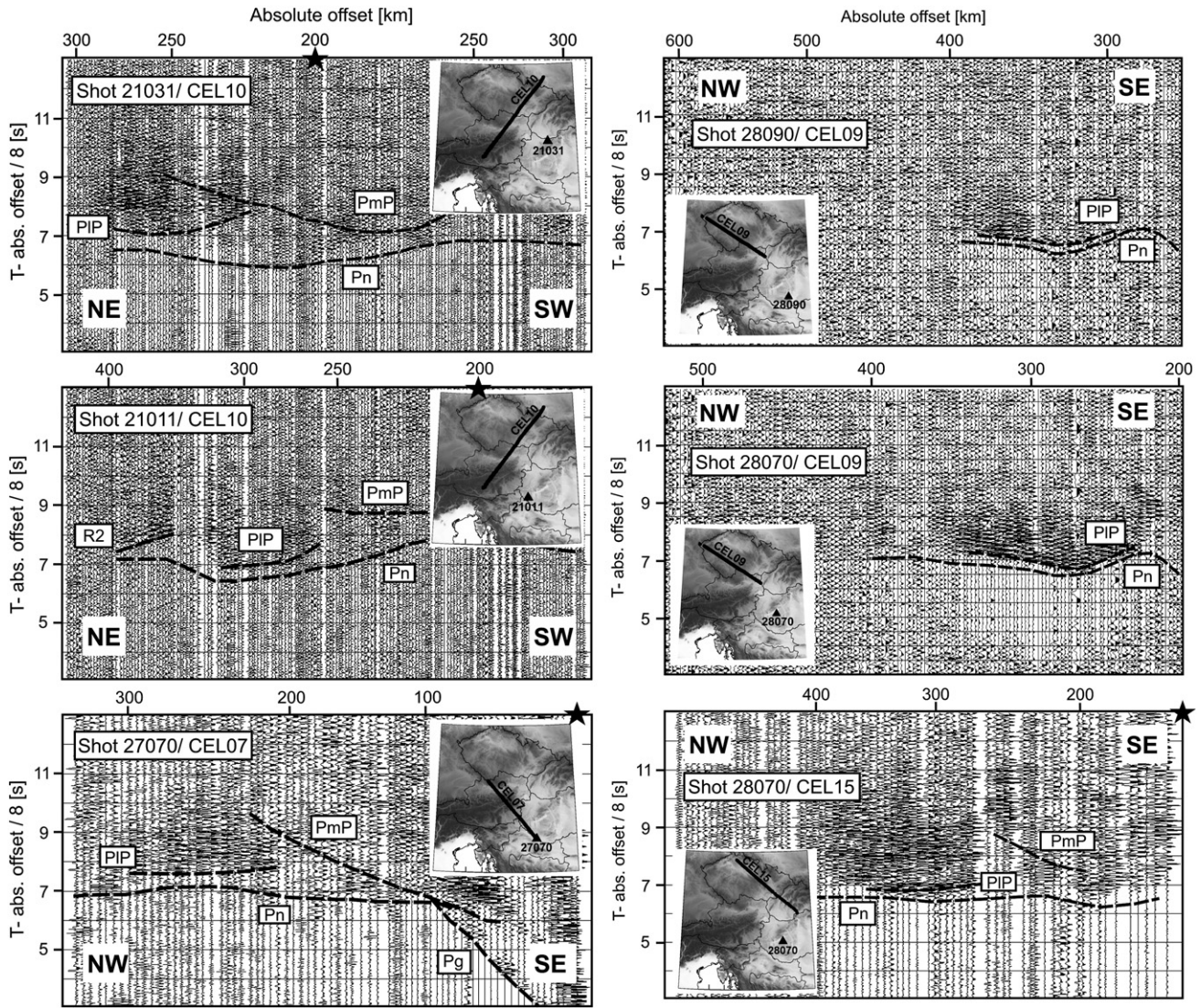


**Fig. 3.** Six seismic sections illustrating reflections from the uppermost mantle (PIP, R2). Other phases: PmP: Reflected wave from the Moho; Pn: Refracted wave from the uppermost mantle. Pg: Diving wave through the crust. The broken lines indicate synthetic travel time curves derived from 3D models (Behm et al., 2007) in case of Pn and PmP phases. PIP and Pg phases are represented by actual travel time picks.

lithosphere/shallow asthenosphere in the Pannonian region comprise frequencies no higher than 8 Hz.

It must be noted that most of the shots are situated in the region of the Pannonian basin. However, not all of them are located in the deep sediments. The fact that the PIP amplitude is stronger than the Pn amplitude also makes it unlikely that PIP represents a refracted wave from the mantle following multiple reflections in the sedimentary basin. The good transmission of seismic energy into the Pannonian lithosphere is also demonstrated in earlier studies (e.g. Hajnal et al., 1996, and references therein) and may be attributed to well-compacted near-surface sediments, where most of the shots were fired below the groundwater table. Further on, a homogeneous and seismically transparent crust and uppermost mantle would facilitate deep penetration of the seismic waves.

**4. Seismic modelling**

We aim to model the depth and shape of a reflecting interface which explains PIP travel times in the region between the Eastern Alps and the Western Carpathians. Due to their rare occurrence, R2 phases are not considered. Several processing steps are performed in order to derive the most plausible model. These include iterative picking of

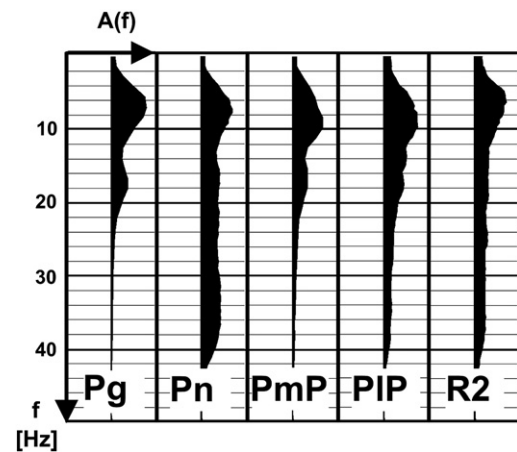


**Fig. 4.** Frequency spectra of four different seismic phases (Pg, Pn, PmP, PIP, R2) for shot 21011. See text for details.

travel times, incorporation of a priori information (crustal velocity structure), forward modelling, and finally, an inversion of the travel times. The inversion results are validated by different tests.

#### 4.1. Initial travel time analyses

A first set of PIP travel times is derived by focussing on offsets between 250 and 350 km, although at some locations, arrivals at larger offsets are also included. Picking of travel times is done after applying a band pass filter (1–2–12–24 Hz) and Automatic Gain control (window length 7 s) to the data. The accuracy of the picking of the onset ranges from 50 ms to 150 ms. However, a much larger source of (systematic) errors is the possible misinterpretation of the phases. Therefore forward modelling is implemented to improve travel time picking (cf. Section 4.3).

#### 4.2. Velocity structure of the crust and upper mantle

The travel times of reflected waves depend on the reflector geometry and the velocity distribution above. Examples of inversion algorithms which simultaneously reconstruct the reflector geometry and the velocity distribution are given by Bleibinhaus and Gebrande (2006) or Hobro et al. (2003). However, for two reasons we prefer to use already existing velocity information which is kept fixed during the inversion. First, the number of PIP travel times does not allow for a useful joint inversion for both velocities and reflector geometry. Second, crustal velocities and the Moho structure have been obtained from thorough analyses of Pg, PmP and Pn waves (Behm et al., 2007). On the other hand, upper mantle velocities are not as well constrained as the crustal structure. Therefore three different upper mantle velocity models are used throughout the following studies. They all have the velocity at the base of the Moho in common (taken from the Pn velocity map in Behm et al., 2007), but differ with respect to the increase of velocity with depth. Based on previous results (Behm et al., 2007; Brückl et al., 2007; Grad et al., 2009), three different vertical velocity gradients of  $0.002 \text{ s}^{-1}$ ,  $0.005 \text{ s}^{-1}$  and  $0.01 \text{ s}^{-1}$  are used. For a 30 km thick layer with a top velocity of 8 km/s, these values result in average velocities of 8.03, 8.06 and 8.15 km/s.

#### 4.3. Forward modelling and final correlation of PIP travel times

In the next step, the aforementioned velocity model is implemented to calculate PIP travel times for horizontal reflectors of a constant depth. The calculated travel times are then displayed on the shot gathers in order to better constrain the possible depth range and to guide improved picking. For travel time calculation, we use a code based on Ray Tracing (Psencik, 1998) and a fast, FD-based Eikonal solver (Hole and Zelt, 1995). The latter is also used in the implemented inversion (cf. Section 4.4). However, the Ray Tracing code has the advantage of allowing the explicit definition of 1st order velocity discontinuities above the reflecting interface (e.g. velocities jump at the Moho) and is therefore regarded as more accurate. Such discontinuities can only be approximated by a velocity gradient zone in case of the Eikonal solver, and the extent of the gradient zone cannot be smaller than the used grid size. Furthermore, the algorithm by Hole and Zelt (1995) is restricted to reflector dips up to  $35^\circ$ .

We calculate PIP travel times for all three vertical mantle velocity gradients and reflector depths of 55, 60, 70 and 80 km by Ray Tracing. Examples are shown in Fig. 5. Despite the assumption of a horizontal reflector simplifying the posed problem, we deduce several constraints from the results. Firstly, forward modelling narrows the possible reflector depth from 50 km to 60 km. We further find an irresolvable trade-off between the velocity gradient and the depth of the reflector. With regard to the picking accuracy, the travel time curve for a reflector depth of 55 km and a mantle gradient of  $0.005 \text{ s}^{-1}$  is indistinguishable from the travel time curve for a depth–gradient

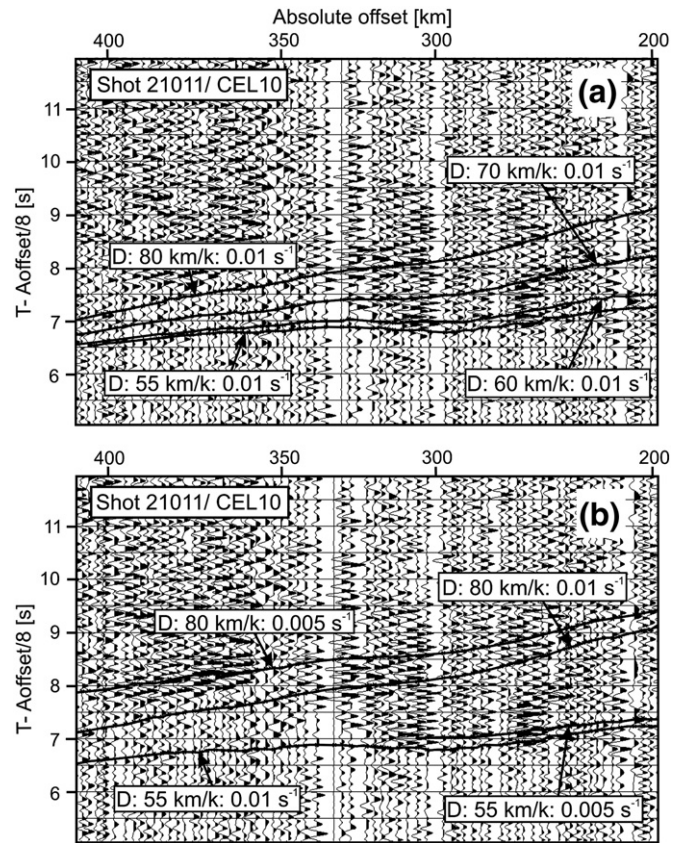


Fig. 5. Comparison between data and results from forward calculation based on Ray Tracing. (a) 4 travel time curves for different reflector depths (55 km, 60 km, 70 km, 80 km) and a constant vertical mantle velocity gradient ( $0.01 \text{ s}^{-1}$ ) (b) 4 travel time curves for different vertical mantle velocity gradients ( $0.005 \text{ s}^{-1}$ ,  $0.01 \text{ s}^{-1}$ ) and different reflector depths (55 km, 80 km). Note the similarity between the travel time curves for the depth/gradient pairs of ( $55 \text{ km}/0.005 \text{ s}^{-1}$ ) and ( $60 \text{ km}/0.01 \text{ s}^{-1}$ ).

combination of  $60 \text{ km}/0.01 \text{ s}^{-1}$ . Thus the mantle velocity cannot be accurately deduced from the curvature of the reflection hyperbola.

#### 4.4. Inversion

Following the procedures outlined in the previous section, 1078 travel times were finally correlated in the shot gathers (Fig. 6). The inversion of these travel times for the depth and shape of the reflector is performed with the code by Zelt et al. (1996). Travel times are calculated for an initial reflector depth model  $Z_0(x,y)$  in a background velocity model. The difference between the observed and the calculated travel times are inverted for depth changes at the reflection points  $(x,y)$ , such that for each travel time residual,  $\delta T$ , a depth change,  $\delta Z$ , is obtained. These depth changes are smoothed (averaged) within a given lateral radius and subsequently interpolated to full coverage. Finally, these interpolated depth changes,  $\delta Z(x,y)$ , are added to  $Z_0(x,y)$  at each location  $(x,y)$ , and an updated reflector depth model,  $Z_1(x,y)$ , is derived. The whole procedure is repeated for the updated reflector depth model until a satisfying fit between observed and calculated travel times is achieved. This is necessary since the relation between the travel time residuals and the shape of the reflecting interface is highly non-linear. The trade-off between the travel time fit and the roughness of the reflector depth model is controlled by the size of the averaging filter, which is decreased at each iteration step. We perform 3 iterations, and the according sizes of the averaging filter are 120 km, 80 km, and 40 km.

The background velocity model is the 3D model described in Section 4.2. The influence of the poorly constrained mantle velocity gradient is taken into account by performing inversions with three

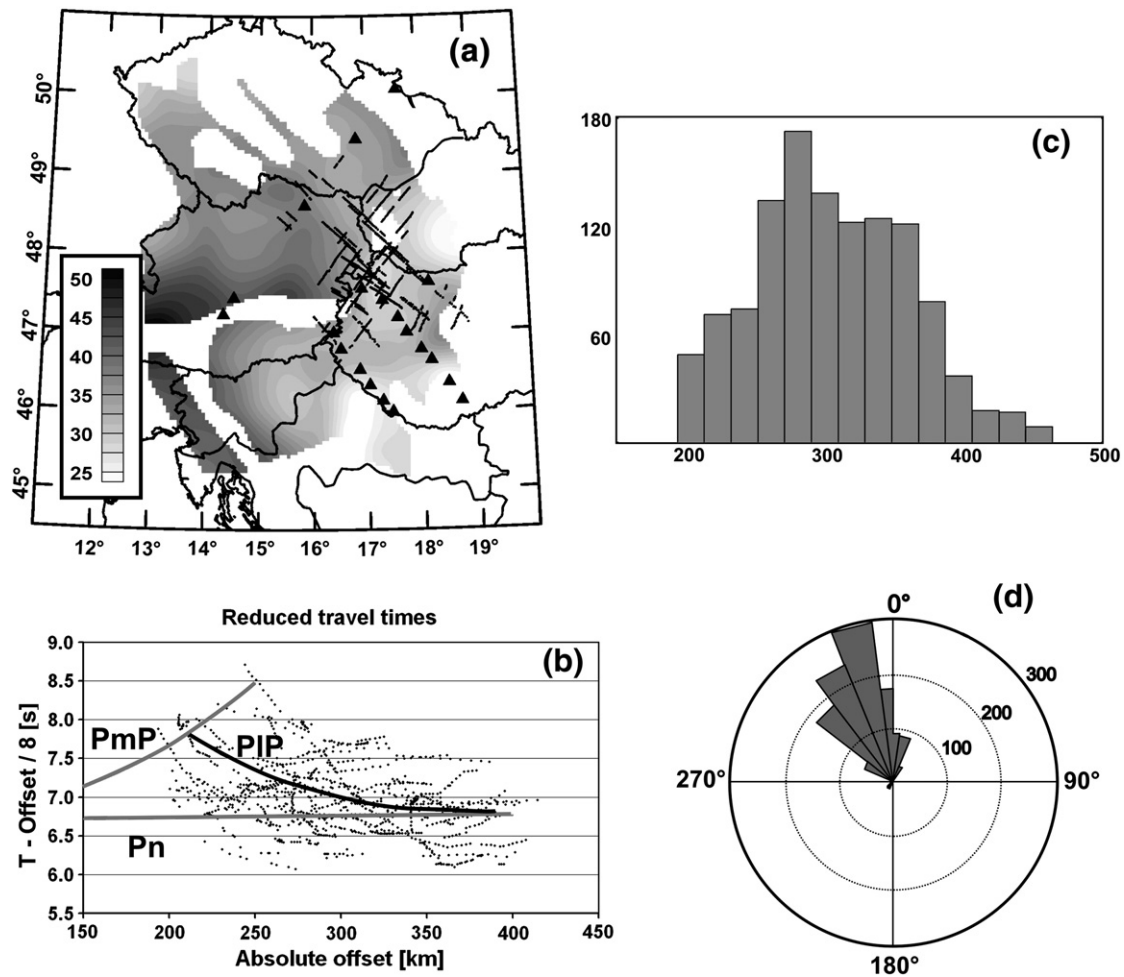


**Fig. 6.** Correlated PIP travel times used for inversion. (a) Shot locations (black triangles) and CMP locations (black dots), superimposed on the Moho depth map [km] by Behm et al. (2007). (b) Linear moveout (LMO) – corrected travel times (LMO velocity 8 km/s) of PIP travel times plotted vs. absolute offset. Solid black line: Best fitting hyperbola for PIP picks. Grey solid lines: Best-fitting travel time curves for PmP and Pn picks from the region. (c) Histogram of PIP travel times vs. absolute offset (d) Rose diagram showing the azimuthal distribution of the correlated PIP travel times. Note the bias towards the north–north–western direction.

different velocity gradients. We also perform an inversion for a 1D background velocity model in order to investigate the significance of the 3D velocity distribution. The 1D model represents an average velocity–depth function of the area with a mantle gradient of  $0.005 \text{ s}^{-1}$ . The initial reflector model is always a plain surface with a constant depth of 55 km. The results are shown in Fig. 7. Table 1 summarises the travel time fit (expressed as the standard deviation of the travel time residuals) of each inversion.

Each solution derived from a 3D background velocity model features the same shape of a roughly 300 km by 200 km wide overall horizontal reflector with an upward directed bulge in its centre. The average depth in the centre varies with the choice of the vertical velocity gradient in the upper mantle. The location of the bulge always coincides with the Little Hungarian Plain. The dip – measured as the steepest descent between the bulge and the outer flanks – is between  $5^\circ$  and  $7^\circ$ . In comparison, the solution obtained from the 1D background velocity model exhibits a different coverage and structure. The reflector dips more steeply ( $10^\circ$ ) to the North-West, and rises to 30 km depth in its easternmost part. In case of the 3D background velocity model, the travel time residuals vary moderately with the different mantle velocity gradients. A gradient of  $0.005 \text{ s}^{-1}$  results in a significantly better travel time fit in the initial model. For this reason, we chose the solution from this inversion (Fig. 7c) as the most plausible result. The solution derived from the 1D background velocity model is disregarded since the standard deviation of the travel time residuals before and after the inversion is much higher

than for all 3D background velocity models. For comparison, it should be noted that the standard deviation of the Pg travel time residuals (diving waves through the crust) is  $0.26 \text{ s}$  (Behm et al., 2007).

In a next step, the influence of the averaging filter is tested. For the 3D background velocity model and the mantle gradient of  $0.005 \text{ s}^{-1}$ , three additional inversions with successively smaller filters are performed (Fig. 8). The filter sizes in the last iteration step are 32, 16 and 8 km, and the corresponding standard deviations of the travel time residuals are 0.3 s, 0.28 s and 0.26 s. In general, the same result as with the previously used filter size of 40 km is achieved. The only notable difference applies to the centre of the bulge where the smaller sized filters result in 2–3 km shallower depths. However, as it is demonstrated in the foregoing analyses, the influence of the still not perfectly constrained background velocity model and possible systematic errors in the correlation of travel times have a larger impact on the inversion result. Thus we prefer to stay on the conservative side and base the next processing steps and interpretations on the reflector depth model shown in Fig. 7c.

#### 4.5. Influence of the initial model

As outlined in the previous section, the inversion routine applies depth changes to reflection points (x,y) in a given model (e.g. the initial model). For a dipping reflector, the reflection points will differ from those of a reflector at constant depth. In case of a constant velocity layer, a dip of  $5^\circ$ , a reflector depth of 55 km at the reflection

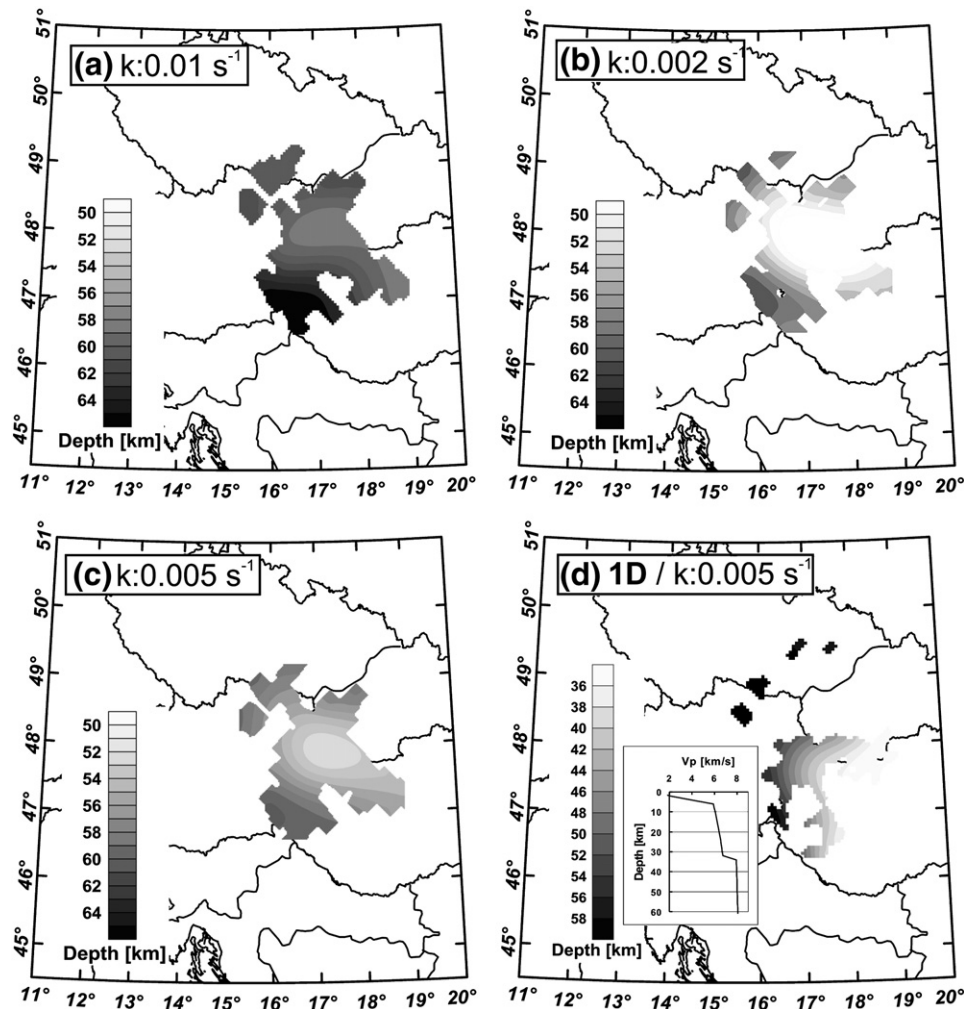


Fig. 7. Results from the inversion of PIP travel times using different background velocity models. (a) 3D model, mantle velocity gradient  $0.01 \text{ s}^{-1}$ . (b) 3D model, mantle velocity gradient  $0.002 \text{ s}^{-1}$ . (c) 3D model, mantle velocity gradient  $0.005 \text{ s}^{-1}$ . (d) 1D model, mantle velocity gradient  $0.005 \text{ s}^{-1}$ . Note the different colour scale in (d).

point, and an offset of 300 km, the reflection point is shifted by 40 km. 3D velocity distributions will add even more non-linearity to this problem. For a limited set of travel times, the convergence towards the correct solution may depend on the choice of the initial model. Therefore we test the influence on the inversion by implementing four additional initial models. Each of them is characterised by a dip of  $5^\circ$  in the centre of the investigated area such that the initial reflector covers a vertical distance of 24 km along a lateral distance of 275 km. The dips are oriented towards North, South, West, and East, respectively. The corresponding standard deviations of the travel time residuals before/after the inversion are (0.51 s/0.31 s), (0.45 s/0.3 s), (0.40 s/0.29 s), and (0.40 s/0.3 s). As the 3D background velocity model with a mantle gradient of  $0.005 \text{ s}^{-1}$  is chosen, we compare the results (Fig. 9) with the preferred solution (Fig. 7c). We do not find any pronounced difference between the results, nor is the position of the bulge shifted. Furthermore, the standard deviations of the travel time residuals prior

to the inversion are always significantly larger for dipping reflectors than for constant depth. Thus we conclude that the overall horizontal appearance of the reflector and the bulge are robust features with respect to the inversion routine.

## 5. Comparison with other studies in the region

### 5.1. Upper mantle structure

Based on upper mantle phases, Sfóda et al. (2006) imaged a reflector below the Western Carpathians which dips steeply ( $\sim 10^\circ$ ) towards the north. The south-westernmost part of this feature starts approximately at the north-easternmost edge of the reflector presented in this study. However, the Western Carpathian reflector is considerably shallower (40 km in the south-westernmost part) and is thus regarded as a different unit. It must also be noted that Sfóda (2010) provides a second explanation for the upper mantle phases which involve diffractions from small-scale heterogeneities at the crust–mantle transition. Hrubcová et al. (2009) found a sub-horizontal mantle discontinuity in depths between 55 and 60 km which tangents the north-western edge of the mantle reflector shown in this paper. Despite the limited seismic data coverage of only one shot recorded along a single profile, the spatial coincidence and the character of this reflector makes it very likely that this mantle-discontinuity is identical to our study object.

Table 1

Summary of the inversion results. SD: Standard deviation of the travel time residuals.

Background velocity model	Mantle gradient [ $\text{s}^{-1}$ ]	SD initial model [s]	SD final model [s]	Average depth after inversion [km]
3D (Fig. 7a)	0.01	0.36	0.35	60
3D (Fig. 7b)	0.002	0.37	0.29	54
3D (Fig. 7c)	0.005	0.32	0.30	50
1D (Fig. 7d)	0.005	0.55	0.38	45

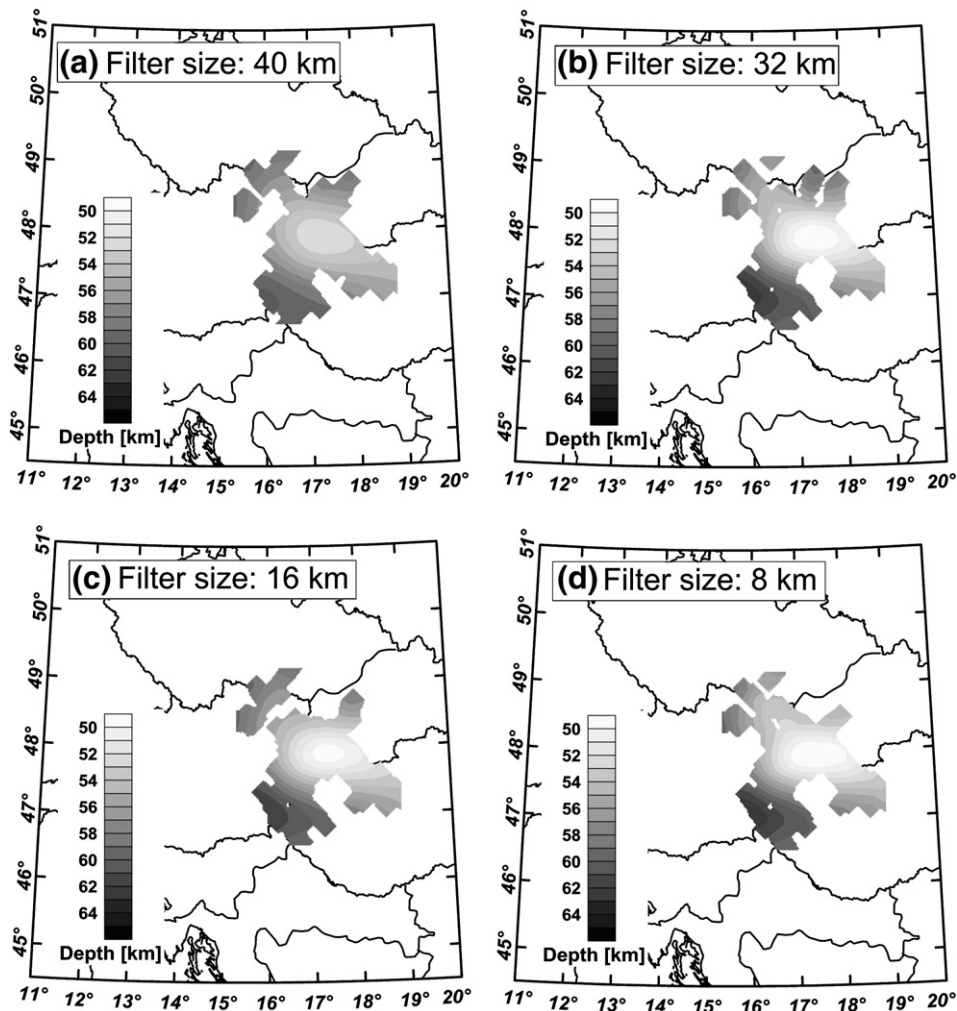


**Fig. 8.** Results from the inversion of PIP travel times using different smoothing filters. 3D background velocity model, mantle velocity gradient  $0.005 \text{ s}^{-1}$ . (a) Filter size 40 km. (b) Filter size 32 km. (c) Filter size 16 km. (d) Filter size 8 km. Model (a) is chosen as the result on which the forthcoming interpretations are based.

Hetényi and Bus (2007) calculated Receiver Functions at four permanent seismic stations in Hungary. The location of the station at Sopron coincides with the south-western flank of the mantle reflector. Although their study focuses on the Moho topography, teleseismic events from the northern and eastern directions may be interpreted for a positive velocity contrast in a depth between 55 and 60 km.

## 5.2. Moho and crustal structure

Behm et al. (2007) showed that the area is characterised by high velocity ( $>7.0 \text{ km/s}$ ) lower crust and Moho depths ranging between 28 and 32 km. However, the Moho structure is not as well constrained as in the surrounding regions, which is also indicated by a lack of coverage in the Moho map. A detailed inspection of these seismic data is given in Fig. 10. In this figure, Offset-Bin-Stacks (OFB stacks) along a south-north oriented profile are shown. The OFB stacks were generated from the seismic traces of the active source experiments, and they are used to derive the 1D seismic structure of specific locations. A single OFB stack includes all traces which have their common mid point close to a defined location. These traces are further stacked in offset bins, and the stacked traces are displayed along their offsets. The result is a 1D representation of the travel time curves of the main crustal phases (Pg, PmP, Pn) at this location. Behm et al. (2007) illustrate the methodological principle in detail and derive a 3D Pg velocity model from all OFB stacks. We use the OFB stacks for qualitative assessment of the crustal structure in our area of interest.

For this purpose, the OFB stacks are displayed with a linear move-out reduction of  $8 \text{ km/s}$  such that refracted waves from the uppermost mantle (Pn phase) align horizontally. Between  $y = 5240$  and  $y = 5300$  the Pn phase can hardly be recognised, but instead, a strong phase with high apparent velocity ( $>7.0\text{--}7.3 \text{ km/s}$ ) is observed. Direction-dependant effects (dipping layers) are ruled out since the OFB stacks result from CMP sorting over the entire azimuth range. By applying 3D tomography, Behm et al. (2007) could verify that these high velocities represent in-situ velocities. We observe that instead of Pn arrivals, phases with velocities lower than usual upper mantle velocities appear, thus the discontinuity at the Moho is replaced by a gradual increase of velocities. Similar observations are reported from regions which are characterised by extensional tectonic settings (e.g., Central Denmark (Thybo et al., 2006) or the Baikal rift (Nielsen and Thybo, 2009)) and can be explained by mafic underplating. This is in accordance with the presence of extensive late Miocene intermediate to acidic and Plio-Pleistocene mafic volcanism in the area (Harangi et al., 1995). Mafic cumulates, the products of underplating, were identified as xenoliths from the near BBH (Embey-Isztin and Scharbert, 1990) and seem to be a general phenomenon in the vicinity of volcanic regions (Kovács et al., 2004). The area with lacking Pn phases and high velocity lower crust coincides with the location of the bulge in the mantle reflector.

Simeoni and Brückl (2009) performed gravity stripping of the area by removing the gravity effect of the upper 10 km of the crust. Assuming standard lower crustal densities, Tierno Ros (2009) modelled the gravity

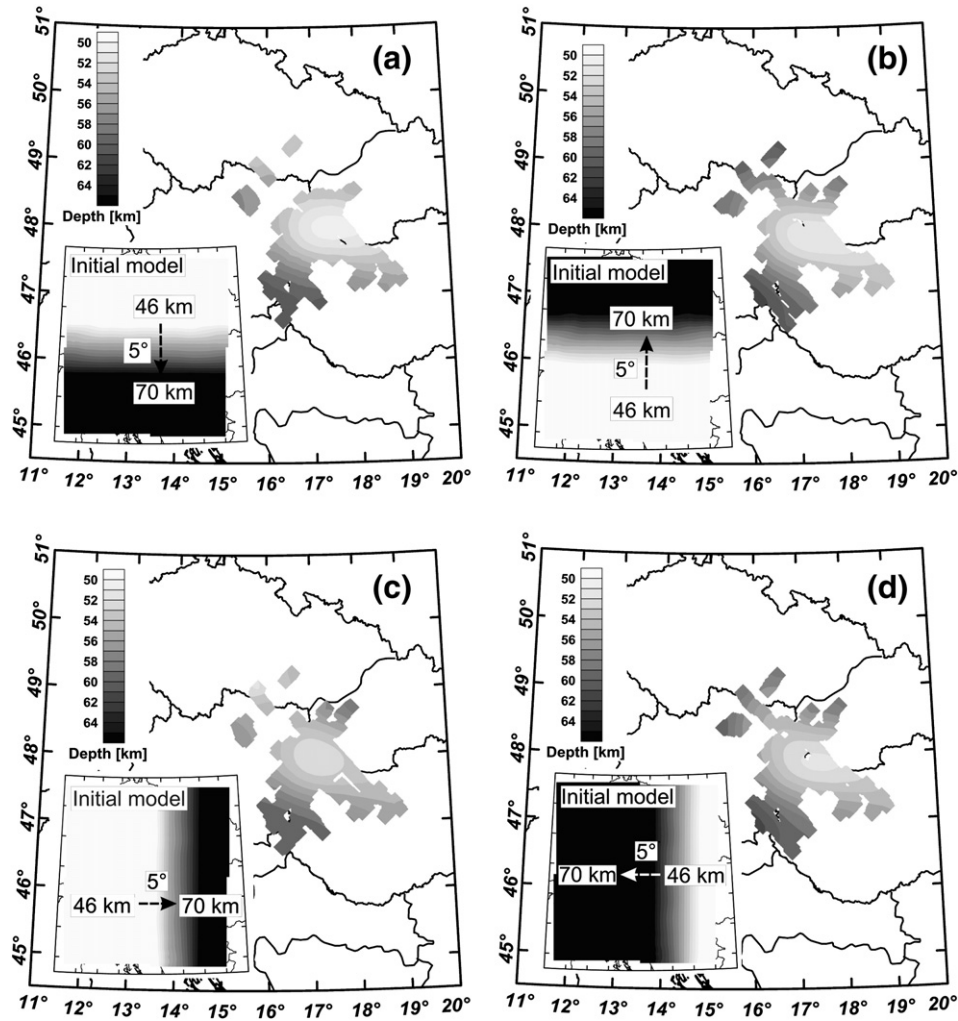


**Fig. 9.** Results from the inversion of PIP travel times using different initial models of reflector depth. 3D background velocity model, mantle velocity gradient  $0.005 \text{ s}^{-1}$ . (a) Southward dipping reflector. (b) Northward dipping reflector. (c) Eastward dipping reflector. (d) Westward dipping reflector. The dip is always  $5^\circ$ . The initial models are displayed in the inserts.

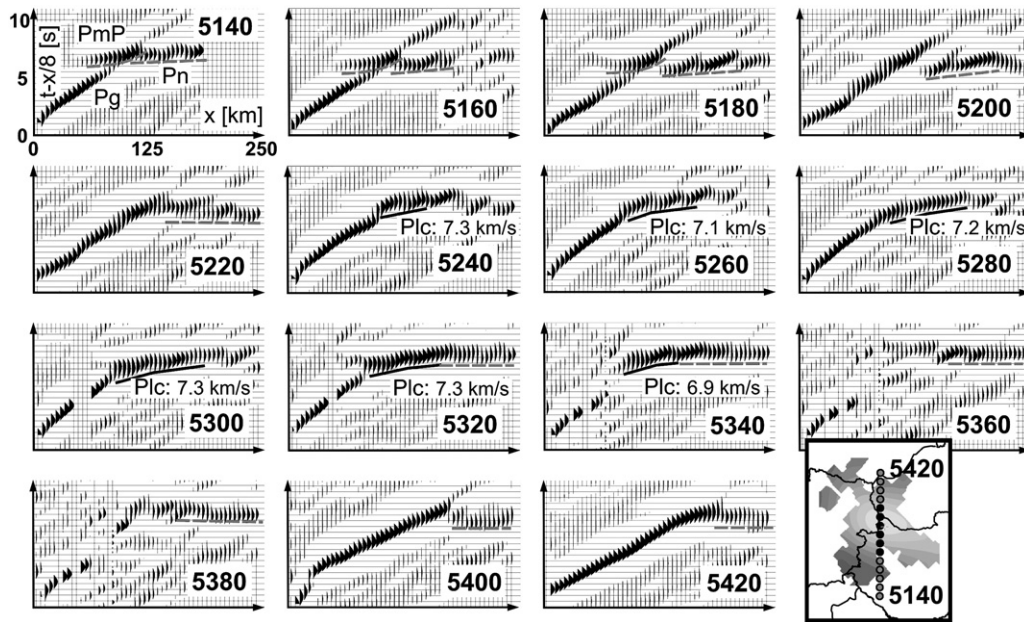


**Fig. 10.** Offset bin stacks (OFB) along a 280 km long south–north oriented profile. See text for details. The distance between the OFB stacks is 20 km. Grey hyperbola (broken lines): PmP arrivals. Grey straight broken lines: Pn arrivals. Black straight line: High-velocity refractions from the lower crust (Plc; apparent velocity calculated from time–distance relationship). The inset in the lower right corner gives the location of the OFB stacks with respect to the mantle reflector. Black dots correspond to locations where high-velocity refractions from the lower crust are observed.



**Table 2**

Overview on the models used in the calculation of reflection amplitudes (Fig. 12). See text for details.

Scenario	Upper layer/Axis of symmetry	Lower layer/Axis of symmetry (anisotropy) OR velocity contrast (isotropy)	Direction of ray
1	Anisotropic/X	Anisotropic/Y	X
2	Anisotropic/X	Anisotropic/X	Y
3	Anisotropic/X	Anisotropic/Y	Y
4	Anisotropic/X	Anisotropic/X	X
5	Isotropic	Isotropic/dV = +0.50 km/s	–
6	Isotropic	Isotropic/dV = +0.25 km/s	–
7	Isotropic	Isotropic/dV = –0.50 km/s	–
8	Isotropic	Isotropic/dV = –0.25 km/s	–

Falus (2004) demonstrated that there are two anisotropically distinct layers in the lithospheric mantle in the nearby Bakony–Balaton Highland (BBH) area. The anisotropy is calculated based on the xenolith deformation statistics and the depth is estimated by using appropriate thermobarometers (Kovács et al., 2011). The shallower layer extends from the Moho (~30 km) to ~45 ± 5 km depth and is characterised by a transpressional deformation pattern and moderate anisotropy ( $V_p$  6.0%,  $V_s$  3.9%). The deeper portion is from ~45 km depth at least to the LAB (~65 km) and shows a deformation pattern characteristic for asthenospheric flow and displays strong anisotropy ( $V_p$  11.6%,  $V_s$  6.5%). In this scenario, the bottom of the shallow layer with moderate anisotropy represents the fossil LAB prior to the extension and the deeper layer with strong anisotropy is the juvenile lithosphere which was added in the thermal relaxation stage following the extension. It is probable that this layering in the lithospheric mantle is not only a local phenomenon but extends over a wider area, and as such, it could be present in the study area which is only 50–100 km northwest of the BBH. Considering the westward dipping LAB and Moho, the boundary between these two distinct layers could coincide with the reflector at 55 km depth. In this case, the PIP phases would result from the change of anisotropy, and the bulge in the reflector could be interpreted as upwelling of the fossil asthenosphere.

It is uncertain whether the difference in anisotropy is large enough to produce the observed reflectivity. Warner and McGearry (1987) postulate that upper mantle anisotropy caused by realistic geological settings can hardly produce significant reflectivity. Barruol and Kern (1996) examined samples from the exposed lower crust in the Ivrea zone and derived an average  $V_p$  anisotropy of 5.6%. For this region, Barruol and Mainprice (1993) also analysed the influence of anisotropy

on the reflection coefficient. They came to the conclusion that anisotropy modifies the reflectivity in a complex way, but overall the reflection coefficient is only slightly enhanced. E.g., the difference to the isotropic case ranges from –0.02 to +0.04.

However, the before mentioned papers describe reflectivity for steep angle seismic data, where the offset is always close to zero. For a wide angle data set like ours, the dependency from the angle of incidence, and thus from the offset, must be taken into account (Zoeppritz equations and geometrical spreading). We use the programme ANRAY (Psencik, 1998) to calculate amplitudes of the displacement vector for different anisotropic and isotropic scenarios. For all models, the crustal structure is defined by the average 1D velocity–depth function of the region and a Moho depth of 30 km. The reflecting interface is located in 55 km depth. The mean mantle velocity at each depth is calculated from  $V_p(z) = 7.93 \text{ km/s} + 0.005 z$ , where  $z$  [km] is the depth below the Moho. The mean shear wave velocity is  $V_s(z) = V_p(z)/1.8$ , which is the assumed  $V_p/V_s$  ratio for mafic mantle rocks (e.g. Brocher, 2005). The programme ANRAY allows specifying a variable density distribution according to  $\rho$  [kg/m<sup>3</sup>] =  $1.7 + V_p$  [km/s] 0.2.

In order to account for the concept of mantle flow, we assume horizontal transverse isotropy (e.g. Stein and Wysession, 2003) for the layers above and below the reflecting interface. By choosing different axes of symmetry (slow axis) for both layers and varying the azimuths and offsets of the rays, we calculate the possible range of amplitudes. The five independent elastic parameters are calculated from the above mentioned mean velocities and the anisotropic parameters given by Falus (2004). Additionally, isotropic scenarios including velocity increase/decrease are also modelled. The eight different scenarios are summarised in Table 2. The results are shown in Fig. 12.

Scenarios 1,2,5, and 6 represent a velocity increase and the others a velocity decrease. Due to the orthogonal orientation of the slow axes in both layers, scenarios 1,3 result in the maximum possible  $V_p$  velocity contrast ( $\pm 0.68$  km/s) in case of anisotropy. If the axes of symmetry are oriented parallel (scenarios 2,4), the maximum  $V_p$  velocity contrast is  $\pm 0.21$  km/s. The velocity increase results in much stronger amplitudes than a velocity decrease. Further, the increase of reflection energy around the critical offset (e.g. 250–270 km for scenarios 2 and 6) and the asymmetry of the amplitude–offset relation correspond roughly with the histogram of correlated PIP travel times (Fig. 6c). Neglecting the influence of the imperfectly modelled crustal structure and the limited accuracy of the reflector depth estimation, we speculate that the velocity contrast at the reflecting interface is around +0.2 km/s. We further conclude that a negative velocity contrast (mafic layers, LAB, fluids) is a rather unlikely cause for the PIP

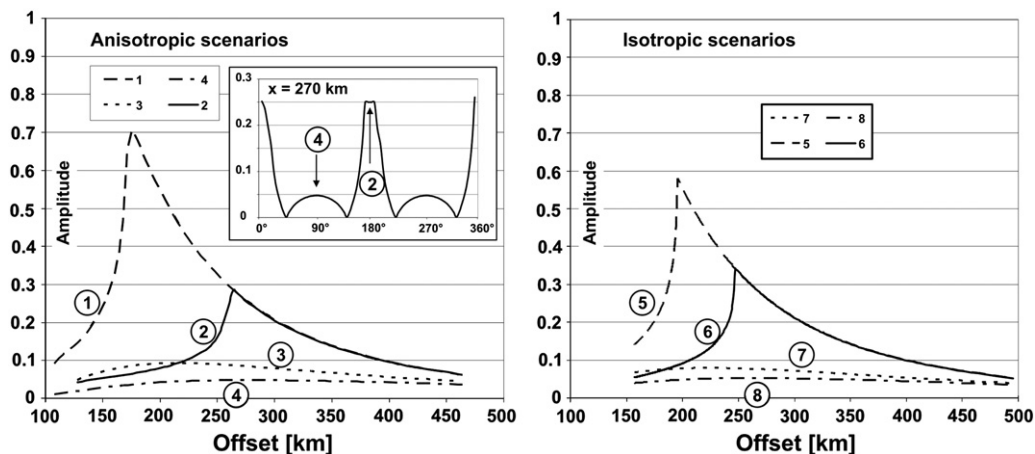


**Fig. 12.** Amplitude vs. offset for the eight different scenarios summarised in Table 2. See text for details. The amplitude includes geometrical spreading, and it is calculated from the modulus of the complex amplitude of the z-component of the displacement vector. Thus it is comparable to the output of a vertical component geophone. All amplitudes are scaled by a constant factor such that the maximum amplitude (scenario 1, offset 175 km) is identical to the reflection coefficient (0.7) at this offset. For comparison, the scaled amplitude of the PmP reflection drops from 4.45 (maximum, offset 80 km) to 0.57 (offset 200 km). The inset in the left figure shows the scaled amplitude vs. the azimuth at the offset  $x = 270$  km when the axes of asymmetry in both layers are parallel (e.g. scenarios 2, 4).

reflections since the pronounced offset-dependant occurrence of PIP travel times doesn't find its expression in the modelled amplitude-offset relation. On the other hand, anisotropy would be in agreement with the pronounced direction-dependant occurrence of reflections (Fig. 6d), and could also generate a positive velocity contrast.

Kovács et al. (2011) provide a review of recent studies on shear wave splitting (SKS) in the wider region of the entire Carpathians and the easternmost Alps. In the centre of our study area, the data indicate a complicated pattern of mantle anisotropy. In the southwest, the NW–SE oriented fast axis is characterised by moderate delays (<0.5 s). Only approximately 50 km to the east, the direction of the fast axis changes to E–W and the delays are higher (0.5 to 1.0 s). Although an interpretation of this pattern is far beyond the scope of this paper, we conclude that changes of mantle anisotropy are significant in the study region. Putting all evidence together, we favour a change in anisotropy as the most likely cause for the mantle reflector.

## 7. Conclusions

Analyses of data from recent wide-angle refraction/reflection experiments reveal a seismic discontinuity in the upper mantle between the Eastern Alps and the Western Carpathians. The inversion of associated travel times yields an overall horizontal and radially slightly dipping reflector in approximately 55 km depth. Amplitude modelling suggests that the reflector represents a positive velocity contrast. We propose a model, where during a first phase of extension in the early/middle Miocene the lithosphere got considerably stretched and thinned. Thermal relaxation in the late Miocene/Pliocene resulted in the addition of juvenile lithosphere. According to xenolith studies, these two lithospheric layers exhibit significantly different seismic anisotropy. The azimuthal distribution of the mantle reflector phases is strongly biased towards the north–north–western direction. Based on this observation and amplitude modelling, we therefore suggest that the mantle reflector represents the boundary between these two layers. Mafic underplating at the Moho level coincides with the location of the mantle reflector. Altogether, the geophysical and geological signatures of the lower crust and upper mantle indicate the entire lithosphere of the region is affected by extension related processes.

## Acknowledgements

We would like to thank Ewald Brückl and Werner Chwatal for fruitful discussion, and Karoline Alten for perfect proof reading of the manuscript. The thoughtful reviews by Piotr Sřoda and Guilhem Barruol provided substantial contributions. György Hetényi and Ivan Pšencik are thanked for discussion of their data and codes. This work was partially supported by a Marie Curie International Reintegration Grant (NAMS-230937), an OTKA research grant (F67917) and a Bolyai Scholarship (2007–2010) to I. Kovács and G. Falus.

## References

- Abramovitz, T., Thybo, H., MONA LISA Working Group, 1998. Seismic structure across the Caledonian Deformation Front along MONA LISA profile 1 in the southeastern North Sea. *Tectonophysics* 288, 153–176. doi:10.1016/S0040-1951(97)00290-4.
- Bada, G., Horváth, F., 2007. Present-day stress field and tectonic inversion in the Pannonian basin. *Glob. Planet. Change* 58 (1–4), 165–180.
- Balling, N., 2000. Deep seismic reflection evidence for ancient subduction and collision zones within the continental lithosphere of northwestern Europe. *Tectonophysics* 329, 269–300.
- Barruol, G., Kern, H., 1996. Seismic anisotropy and shear wave splitting in the lower crustal/upper mantle transition (lvrea Zone): experimental and calculated data. *Phys. Earth Planet. Int.* 95, 175–194 doi:10.1016/0031-9201(1095)03124-03123.
- Barruol, G., Mainprice, D., 1993. 3D seismic velocities calculated from LPOs and reflectivity of a lower crustal section – example of the Val Sesia (lvrea Zone, Northern Italy). *Geophys. J. Int.* 115, 1169–1188 doi:10.1111/j.1365-1246X.1993.tb01519.x.
- Behm, M., Brückl, E., Chwatal, W., Thybo, H., 2007. Application of stacking and inversion techniques to 3D wide-angle reflection and refraction seismic data of the Eastern Alps. *Geophys. J. Int.* 170, 275–298.
- Best, M., 2003. *Igneous and Metamorphic Petrology*, 2nd edition. Blackwell.
- Bleibinhaus, F., Gebrande, H., 2006. Crustal structure of the Eastern Alps along the TRANSALP profile from wide-angle seismic tomography. *Tectonophysics* 414, 51–69.
- Brewer, J.A., Matthews, D.H., Warner, M.R., Hall, J., Smythe, D.K., Whittington, R.J., 1983. BIRPS deep seismic reflection studies of the British Caledonides. *Nature* 305, 206–210. doi:10.1038/305206a0.
- Brocher, T., 2005. Empirical relation between elastic wavespeeds and density in the earth's crust. *Bull. Seismol. Soc. Am.* 95 (6), 2081–2092.
- Brückl, E., Bodoky, T., Hegedűs, E., Hrubcová, P., Gosar, A., Grad, M., Guterch, A., Hajnal, Z., Keller, G.R., Špičák, A., Sumanovac, F., Thybo, H., Weber, F., ALP 2002 Working Group, 2003. ALP 2002 seismic experiment. *Stud. Geoph. Geod.* 47, 671–679.
- Brückl, E., et al., 2007. Crustal structure due to collisional and escape tectonics in the Eastern Alps region based on profiles Alp01 and Alp02 from the ALP 2002 seismic experiment. *J. Geophys. Res.* 112, B06308. doi:10.1029/2006JB004687.
- Brückl, E., Behm, M., Decker, K., Grad, M., Guterch, A., Keller, G.R., Thybo, H., 2010. Crustal structure and active tectonics in the Eastern Alps. *Tectonics* Vol. 29, TC2011. doi:10.1029/2009TC002491.
- Carbonell, R., 2004. On the nature of mantle heterogeneities and discontinuities: evidence from a very dense wide-angle shot record. *Tectonophysics* 388, 103–117.
- Christensen, N., Mooney, W., 1995. Seismic velocity structure and composition of the continental crust: a global view. *J. Geophys. Res.* 100 (No. B7), 9761–9788.
- Csontos, L., Vörös, A., 2004. Mesozoic plate tectonic reconstruction of the Carpathian region. *Palaeogeogr. Palaeoclimatol. Palaeoecol.* 210 (1), 1–56.
- Embey-Isztin, A., Scharbert, H.G., 1990. Mafic granulites and clinopyroxenite xenoliths from the Transdanubian Volcanic Region (Hungary) – implications for the deep-structure of the Pannonian Basin. *Mineralog. Mag.* 54 (376), 463–483.
- Falus, G., 2004. *Microstructural Analysis of Upper Mantle Peridotites: Their Application in Understanding Mantle Processes During the Formation of the Intra-Carpathian Basin System*. PhD Thesis, Lithosphere Fluid ResearchLab, Eötvös University, Budapest, p. 163.
- Falus, G., Szabó, C., 2000. Mantle upwelling within the Pannonian Basin: evidence from xenolith lithology and mineral chemistry. *Terra Nova* 12 (6), 295–302.
- Falus, G., Szabó, C., 2007. Symplectite in spinel lherzolite xenoliths from the Little Hungarian Plain, Western Hungary: a key for understanding the complex history of the upper mantle of the Pannonian Basin. *Lithos* 94 (1–4), 230–247.
- Fodor, L., Csontos, L., 1999. Tertiary tectonic evolution of the Pannonian basin system and neighbouring orogens: a new synthesis of paleostress data. In: Durand, B., Jolivet, L., Horváth, F., Séranne, M. (Eds.), *The Mediterranean Basins: Tertiary Extensions Within the Alpine Orogen*. Geological Society, London, Special Publication, 156, pp. 295–334.
- Grad, M., Guterch, A., Keller, R.G., Janik, T., Hegedűs, E., Vozar, J., Slaczká, A., Tiira, T., Yliniemi, J., 2006. Lithospheric structure beneath trans-Carpathian transect from Precambrian platform to Pannonian basin: CELEBRATION 2000 seismic profile CEL05. *J. Geophys. Res.* 111, B03301. doi:10.1029/2005JB003647.
- Grad, M., Brückl, E., Majdanskı, M., Behm, M., Guterch, A., CELEBRATION 2000, ALP 2002 Working Groups, 2009. Crustal structure of the Eastern Alps and their foreland: Seismic model beneath the CEL10/Alp04 profile and tectonic implications. *Geophys. J. Int.* 177, 279–295. doi:10.1111/j.1365-246X.2008.04074.x.
- Guterch, A., Grad, M., Keller, G.R., Posgay, K., Vozár, J., Špičák, A., Brückl, E., Hajnal, Z., Thybo, H., Selvi, O., CELEBRATION 2000 Experiment Team, 2003. CELEBRATION 2000 Seismic Experiment. *Stud. Geoph. Geod.* 47, 659–669.
- Haas, J., Mioc, P., 2000. Complex structural pattern of the Alpine–Dinaridic–Pannonian triple junction. *Int. J. Earth Sci.* 89 (2), 377–389.
- Hajnal, Z., Reilkoff, B., Posgay, K., Hegedűs, E., Takács, E., Asudeh, I., Mueller, St. Ansoerge, J., Delaco, R., 1996. Crustal-scale extension in the central Pannonian basin. *Tectonophysics* 264, 191–204. doi:10.1016/S0040-1951(96)00126-6.
- Hansen, T.M., Balling, N., 2004. Upper mantle reflectors: modelling of seismic wavefield characteristics and tectonic implications. *Geophys. J. Int.* 157, 664–682.
- Harangi, S., Wilson, M., Taroni, S., 1995. Petrogenesis of Neogene potassic volcanic rocks in the Pannonian Basin. *Acta Vulcanologica* 7, 125–134.
- Hetényi, G., Bus, Z., 2007. Shear wave velocity and crustal thickness in the Pannonian Basin from receiver function inversions at four permanent stations in Hungary. *J. Seismol.* 11, 405–414. doi:10.1007/s10950-007-9060-4.
- Hobro, J.W.D., Singh, S.C., Minshull, T.A., 2003. Three-dimensional tomographic inversion of combined reflection and refraction seismic data. *Geophys. J. Int.* 152, 79–93.
- Hole, J., Zelt, B., 1995. 3-D finite-difference reflection travel times. *Geophys. J. Int.* 121, 427–434.
- Horváth, F., Bada, G., Szafián, P., Tari, G., Ádám, A., Cloethingh, S., 2006. Formation and deformation of the Pannonian basin: constraints from observational data, in *European Lithosphere Dynamics*. *Mem. Geol. Soc.* 32, 129–145.
- Hrubcová, P., Sřoda, P., Špičák, A., Guterch, A., Grad, M., Keller, G.R., Brückl, E., Thybo, H., 2005. Crustal and uppermost mantle structure of the Bohemian Massif based on CELEBRATION 2000 data. *J. Geophys. Res.* 110, B11305. doi:10.1029/2004JB003080.
- Hrubcová, P., Sřoda, P., Geissler, W.H., SUDETES 2003 Working Group, 2009. From the Variscan to the Carpathians – crust and uppermost mantle structure along the refraction and wide-angle reflection S04 profile of the SUDETES 2003 experiment. *Geophys. Res. Abstr.* 11, EGU2009–EGU12036.
- Kovács, I., Csontos, L., 2007. Paleogene–early Miocene igneous rocks and geodynamics of the Alpine–Carpathian–Pannonian–Dinaric region: an integrated approach. In: Beccaluva, L., Bianchini, G., Wilson, M. (Eds.), *Cenozoic Volcanism in the Mediterranean Area*. Geological Society of America Special Paper, 418.
- Kovács, I., Szabó, Cs., 2008. Middle Miocene volcanism in the vicinity of the Middle Hungarian zone: evidence for an inherited enriched mantle source. *J. Geodyn.* 45, 1–17.
- Kovács, S., Szederkényi, T., 2000. Tectonostratigraphic terranes in the pre-neogene basement of the Hungarian part of the Pannonian area. *Acta Geol.* 43 (3), 225–328.

- Kovács, I., Zajacz, Z., Szabó, Cs., 2004. Type-II xenoliths and related metasomatism from the Nograd-Gomor Volcanic Field, Carpathian–Pannonian region (northern Hungary-southern Slovakia). *Tectonophysics* 393 (1–4), 139–161.
- Kovács, I., Falus, G., Hidas, K., Szabó, Cs., Flower, M.F.J., Hegedüs, E., K.1, Posgay, Zilahi-Sebess, L., 2011. Seismic anisotropy and deformation patterns in upper mantle xenoliths from the central Carpathian–Pannonian region: indications for a collision driven asthenospheric flow? in revision *Tectonophysics*.
- Lenkey, L., 1999. Geothermics of the Pannonian Basin and its bearing on the tectonics of basin evolution. PhD thesis, Vrije Universiteit Amsterdam.
- Majdański, M., Grad, M., Guterch, A., SUDETES 2003 Working Group, 2006. 2-D seismic tomographic and ray tracing modelling of the crustal structure across the Sudetes Mountains basing on SUDETES 2003 experiment data. *Tectonophysics* 413, 249–269.
- Matte, P., Maluski, H., Rajlich, P., Franke, W., 1990. Terrane boundaries in the Bohemian Massif: Result of large-scale Variscan shearing. *Tectonophysics* 177, 151–170.
- MONA LISA Working Group, 1997. MONA LISA – Deep seismic investigations of the lithosphere in the southeastern North Sea. *Tectonophysics* 269, 1–19. doi:10.1016/S0040-1951(96)00111-4.
- Nielsen, Ch., Thybo, H., 2009. Lower crustal intrusions beneath the southern Baikal Rift Zone: evidence from full-waveform modelling of wide-angle seismic data. *Tectonophysics* 470, 298–318.
- Okure, M.S., McBride, J.H., 2006. Deep seismic reflectivity beneath an intracratonic basin: insights into the behavior of the uppermost mantle beneath the Illinois basin. *Precambrian Res.* 149, 99–125.
- Posgay, K., Hegedüs, E., Timar, Z., 1990. The identification of mantle reflections below Hungary from deep seismic profiling. *Tectonophysics* 173, 379–385.
- Posgay, K., Bodoky, T., Hegedüs, E., Kovácsvölgyi, S., Lenkey, L., Szafián, P., Takács, E., Tímár, Z., Varga, G., 1995. Asthenospheric structure beneath a Neogene basin in southeast Hungary. *Tectonophysics* 252, 467–484. doi:10.1016/00401951(95)00098-4.
- Price, C.E., Morgan, J.V., Warner, M.R., Barton, P.J., Jones, K.A., Morgan, R.P., II, 1996. Waveform inversion of deep seismic reflection data: the polarity of mantle reflections. *Tectonophysics* 264, 235–247. doi:10.1016/S0040-1951(96)00129-1.
- Psencik, I., 1998. Package ANRAY, version 4.10. *Seismic Waves in Complex 3-D Structures*. Report 7, 403–404. Dept. of Geophysics, Charles University Prague. Online at <http://sw3d.mff.cuni.cz>.
- Ratschbacher, L., Frisch, W., Linzer, H.G., Merle, O., 1991. Lateral extrusion in the Eastern Alps. 2: structural analysis. *Tectonics* 10, 257–271. doi:10.1029/90TC02623.
- Schmid, S., Fügenschuh, B., Kissling, E., Schuster, R., 2004. Tectonic map and overall architecture of the Alpine orogen. *Swiss J. Geosci.* 97, 93–117.
- Schmid, S.M., Bernoulli, D., Fügenschuh, B., Matenco, L., Schuster, R., Schefer, S., Tischler, M., Ustaszewski, K., 2008. The Alpine–Carpathian–Dinaridic orogenic system: correlation and evolution of tectonic units. *Swiss J. Geosci.* 101, 139–183. doi:10.1007/s00015-008-1247-3.
- Seghedi, I., Downes, H., 2004. Neogene–Quaternary magmatism and geodynamics in the Carpathian–Pannonian region: a synthesis. *Lithos* 72 (3–4), 117–146.
- Simeoni, O., Brückl, E., 2009. The effect of gravity stripping on the resolution of deep crustal structures in the Eastern Alps and surroundings Regions. *Austr. J. Earth Sci.* 102/2, 157–169.
- Sfoda, P., 2010. The bright spot in the West Carpathian upper mantle: a trace of the Tertiary plate collision—and a caveat for a seismologist. *Geophys. J. Int.* 182 (1), 1–10. doi:10.1111/j.1365-246X.2006.03104.x.
- Sfoda, P., Czuba, W., Grad, M., Guterch, A., Tokarski, A.K., Janik, T., Rauch, M., Keller, G.R., Hegedüs, E., Vozar, J., CELEBRATION 2000 Working Group, 2006. Crustal and upper mantle structure of the Western Carpathians from CELEBRATION 2000 profiles CEL01 and CEL04: seismic models and geological implications. *Geophys. J. Int.* 167 (2), 737–760. doi:10.1111/j.1365-246X.2006.03104.x.
- Steer, D.N., Knapp, J.H., Brown, L.D., 1998. Super-deep reflection profiling: exploring the continental mantle lid. *Tectonophysics* 286, 111–121. doi:10.1016/S0040-1951(97)00258-8.
- Stein, S., Wysession, M., 2003. *An Introduction to Seismology, Earthquakes, and Earth Structure*. Blackwell.
- Szafián, P., Horváth, F., 2006. Crustal structure in the Carpatho–Pannonian region: insights from three-dimensional gravity modelling and their geodynamic significance. *Int. J. Earth Sci.* 95 (1), 50–67.
- Thybo, H., Sandrin, A., Nielsen, L., Lykke-Andersen, H., Keller, G.R., 2006. Seismic velocity structure of a large mafic intrusion in the crust of central Denmark from project ESTRID. *Tectonophysics* 420, 105–122.
- Tierno Ros, C., 2009. 3D density modelling of the crustal structure in the Vienna Basin region. Diploma thesis, Vienna University of Technology.
- Warner, M., McGeary, S., 1987. Seismic reflection coefficients from mantle fault zones. *Geophys. J. R. astr. SOC.* 89, 223–230.
- Zajacz, Z., Kovács, I., Szabó, Cs., Werner, H., Pettko, T., 2007. Insights into the evolution of mafic alkaline melts crystallized in the uppermost lithospheric mantle of the Nograd-Gömör Volcanic Field (Northern Hungary): a melt inclusion study. *J. Petrol.* 48 (5), 853–883.
- Zelt, B.C., Ellis, R.M., Clowes, R.M., Hole, J.A., 1996. Inversion of three-dimensional wide-angle seismic data from the southwestern Canadian Cordillera. *J. Geophys. Res.* 101, 8503–8529.